C-band Backscatter Measurements of Winter sea ice in the Weddell Sea, Antarctica

Mark R. Drinkwater

Jet Propulsion Laboratory,
California institute of Technology
4800 Oak Grove Drive
CA 91109, USA

Reza Hosseinmostafa and Prasad Gogineni

Remote Sensing Laboratory
Kansas University
Lawrence, KA

Abstract.

During the Winter Weddell Gyre Study, a 4.3 GHz frequency-modulated continuous-wave (FM-CW) radar scatterometer was operated from the port rail of the German ice-breaker R/V *Polarstern* to obtain detailed shipborne C-band backscatter measurement scans of Antarctic sea ice. The dual polarization radar, which acquired like- (VV) and cross-pol (HV) data at a variety of incidence angles (10-750), was used to record the sea-ice microwave scattering properties during the 1992 austral winter. Calibrated data were recorded for several ice types as the icebreaker crossed the Weddell Sea and at each site, measurements were also made of snow and sea ice characteristics. Meteorological information, radiation budget and oceanographic data were also recorded, The primary scattering contributions under cold winter conditions arise from the air/snow and snow/ice interfaces. Observations indicate some similarities with of Arctic sea ice scattering signatures although the primary difference is in the observation of generally lower mean signatures in the Weddell Sea. This is due to the younger mean ice age and thickness, and correspondingly higher mean salinities. Predominantly white ice forms found in 1992 in divergent areas within the Weddell Gyre ice pack are also generally less rough and deformed than their Arctic counterpart. Comparisons of field scatterometer data with calibrated ERS-1 image show close correspondence, and indicate that rough first-year and older second-year ice forms do not produce distinctively different scattering signatures as in the Arctic. Thick deformed first-year and second-year ice forms on the other hand are clearly discriminated from younger undeformed ice, thereby allowing successful separation of thick and thin ice forms. Time-series data also indicate C-band is sensitive to snow and ice physical changes as a result of climatic and oceanographic forcing, together with the surface heat flux environment.

Key Words: C-band Scatterometer, Winter Weddell Gyre Study, Sea Ice Microwave Scattering

1. IN'IWODUCTION

Annual growth of Southern Ocean sea ice over an area of about 20 million km^2 requires that spaceborne microwave remote sensing be employed as the only practical method to monitor the extent and characteristics of this winter Antarctic sea ice cover. Formation of an extensive ice cover around Antarctica is intimately linked to water mass modification and blending processes by salivating the upper ocean and creating buoyancy gradients. Resulting vertical thermohaline fluxes and large-scale circulation within the zone between the Antarctic polar front and the continental margin together influence the overall hydrographic characteristics of the Southern Ocean (Gordon and Huber, 1990). Observations and theory confirm that the marginal stability of the winter mixed layer in regions such as the Eastern Weddell Sea can be upset by a modest increase in the salt flux from enhanced sea-ice formation in leads and polynyas. Such sea ice features represent holes in the insulating sea ice blanket and can modulate the horizontal and vertical thermohaline and freshwater fluxes of this region. Significant convective events such as that encouraged by the Weddell Polynya (Carsey, 1980; Gordon, 1991) released large amounts of heat and moisture into the atmosphere and provided sufficient enhancement of cooling and ventilation for the production of Antarctic Bottom Water. Knowing the regional distribution of open water, and leads and sea ice is a critical scientific requirement with respect to accurate calculations of horizontal and vertical thermohaline fluxes in the Southern Ocean.

Satellite-borne microwave radars will yield uninterrupted hi-polar sea-ice coverage for the next decade and beyond (Carsey *et al., 1992).* Currently, the 5.3 GHz (C-band) ERS- 1 synthetic aperture radar (SAR) is the only instrument capable of acquiring all-weather (day or night), frequent repeat, high-resolution (20m) Antarctic sea-ice image data; but, this dataset is limited to areas covered by existing receiving stations. As an alternative, the ERS-1 scatterometer data enables generation of an intermediate resolution image product (12 km), but images the entire Southern Ocean (Drinkwater *et* al., 1993a). This study focuses on placing into context C-band microwave signatures obtained using these different systems. In this paper we illustrate field-measured backscattering signatures acquired in regions of different ice characteristics such that coincident images from ERS- 1 can be interpreted. The ultimate scientific goal is to use the tools which remote sensing offers to evaluate the relationship between the changing basin-wide distribution of sea ice and surface fluxes of heat, salt, freshwater and momentum.

2. THE WINTER WEDDELL GYRE STUDY

The Winter Weddell Gyre Study (WWGS '92) was the second austral winter experiment in a series of ongoing investigations of the Weddell Gyre. It was conducted by German, U.S., English and Canadian investigators on-board the German ice-breaking research vessel R/V *Polarstern.* One specific unique element of this cruise was that it was conducted with simultaneous

observations of the sea ice and surface of the ocean in the Weddell Sea by the ERS - 1 satellite SAR. This was the first ever active microwave image data to be recorded of winter sea ice in Antarctica by a satellite-borne radar.

2.1 Satellite Image Data

The ERS- 1 spacecraft routinely collected data over the WWGS '92 study region shown in Figure 1. The active microwave instrument (AMI) acquired data in its SAR and Wind Scatterometer modes. The former is a high-bit-rate data stream requiring direct downlink to and recording at the nearest ground receiving station. SAR data acquisition throughout the experiment (between June and August) was facilitated by the German Antarctic Receiving Station (GARS) site at the General Bernardo O'Higgins Base, which is located at the northern end of the Antarctic peninsula. Simultaneously, SSM/I data and AVHRR data were collected for comparison with SAR imagery. During satellite data acquisition a program of shipborne active and passive microwave observations, coupled with *in-situ* measurements allowed investigation of the microwave signature of various key Antarctic sea ice forms.

2.2 Field Scatterometer and Sea-Ice Surface Measurements

A University of Kansas C-band field-scatterometer instrument (Figure 2) was operated during WWGS '92 from the port rail of *R/V Polarstern* to measure microwave backscattering characteristics of Antarctic sea ice. When the ship was stationary in pack ice, the radar was scanned to obtain independent samples of sea-ice backscatter coefficient (σ°) as a function of incidence angle (θ) and polarization. In support, detailed surface measurements were made within the radar footprint each time a radar scan was completed. Measurements were made of the physical, chemical and dielectric properties of the snow and sea ice, and of the surface heat fluxes. Field sampling along the ship track provided validation data for simultaneous satellite ERS- 1 C-band SAR observations (at $20^\circ \leq \theta \leq 26^\circ$) and enabled collection of a catalogue of 'snap-shot' microwave signatures.

Short 3-4 hour ice stations shown in Figure 1 enabled radar and snow and ice measurements of a number of ice types characteristic of the winter Weddell Sea ice cover (Drinkwater *et al.* 1993 b). A 3-day long ice station from 21-24 July, 1992 also enabled time-series σ° measurements. As well as periodic scans of data over the complete range of incidence angles, the radar was operated at frequent intervals (- 4 hourly) at $\theta = 45^\circ$. At this angle σ° is sensitive to the surface reflectivity and roughness, and also to volume scattering within the snow and ice surface. These data provide a chance to quantify changes in σ° as the heat flux and vapour flux regime varied over the period, and as the physical properties of the snow and ice changed. Examples of data from the short stations shown in Figure 1, and from the 3-day long station, are shown in the following sections.

3. THE RADAR SCATTEROMETER

The Kansas University scatterometer was a low power, triple-antenna, FM-CW (frequency - modulated, continuous-wave) radar altimeter modified to perform ship-mounted backscatter measurements (see Table 1). It operated at a C-band center frequency of 4.3 GHz and was capable of like- (vv) and cross-polarized (hv) measurements. The antenna cluster consisted of; a parabolic dish transmitting antenna fixed at vertical linear polarization, a horn antenna for receiving linear like-polarized signals, and a stripline antenna for receiving cross-polarized signals. This cluster was mounted orthogonal to the ship's rail facing to port (see Figure 2) and was fixed in azimuth but hinged and steerable in the elevation plane by an actuator. A pendulum, fixed in an orientation boresighted with the antennas, provided a simple digital readout calibrated to incidence angle, enabling measurements at precise incidence angles ($10° \leq \theta \leq 75°$) from a workstation inside the ship. The height above the sea ice surface varied as a function of the ship's draft on a day to day basis (with a mean height $H = 16.7$ m).

The scatterometer system is divided physically into two parts; a transmitter/receiver section, and a data acquisition section. The former was located in a weatherproof box directly behind the antenna plate (Figure 2) to minimize the power loss through cables linking the antenna feeds and the transmitter/received unit. The received signals are carried along cables to the data acquisition system located in an indoor work area. A block diagram of the system is shown in Figure 3.

3.1 Transmitter and Receiver Subsystem

Output from the transmitter is frequency-modulated using a triangular wave function. This signal is subdivided into two parts: the first part is fed into the local oscillator port of the mixer, and the second is mixed with a fixed delay-line and coupled into calibration loops. The calibration loop, consisting of calibration IF input from the mixer, IF gain stages, and the modulator, controls the modulation rate to maintain constant calibration IF frequency. The remaining portion of the transmitted signal propagates from the transmitting antenna through space to the target where some of its energy is scattered back in the direction of the radar. This backscattered signal is collected by the receiving antenna and down-converted, filtered, amplified and fed into the data acquisition section of the radar system.

3.2 Data Acquisition Subsystem

The radar was controlled by a Texas instruments personal computer (PC) equipped with a special Digital Signal Processing (DSP) board and the data were stored digitally on hard disk by the PC and independently by a Hewlett Packard Signal Analyzer (HP35680A). The signal analyser provided the magnitude and phase of the signal recorded by the PC together with independent data storage. Recorded data were processed and viewed in real-time using the DSP board and the bandwidth could be selected to optimise the range resolution. The recorded signal was band-pass

filtered to separate the target from the background clutter and converted to independent samples of received power. Internal calibration was performed using direct measurements of the power using the Signal Analyser together with recording the transmitted power directly on the PC. External Calibration was performed by measuring the scattering cross-section of a standard Luneberg Lens target. Further corrections were performed afterwards by coherent subtraction of internal reflections and reflections from the ship's side, together with removal of system artifacts and antenna separation effects. These are described in more detail as follows;

3.3 Backscatter Measurements

Backscattering of the transmitted pulses takes place from the sea ice and the mean received power P_r is expressed as

$$P_r = \frac{\lambda^2}{(4\pi)^3} \int_{area\ illuminated} \frac{P_t G\, \sigma^o}{R^4} dA \tag{1}$$

where P_t is the transmitter power, G is the gain of the transmitting antenna R *is* the range to the target, λ is the wavelength, and σ^o is the normalised backscatter coefficient of the target area (i.e. the average value of the cross-section per unit area).

Beam Pattern Corrections

Measurements are corrected for the shape of the beam of the transmitting and receiving antennas and the resulting illuminated area (after Gogineni *et* al., 1990). For an extensive target the radar returned power is

$$P_r = \frac{P_t G_{t\max} G_{r\max} \lambda^2}{(4\pi)^3} \int_0^{\pi} \int_0^{2\pi} \frac{g_t g_r \sigma^o(\theta,\phi)}{R'} dA \tag{2}$$

where G_{tmax} and G_{tmin} are the maximum gains and g_t and g_r are the relative gain functions of the transmit and receiving antennas, respectively. The above equation is generalised assuming that σ^o is independent of the azimuth angle ϕ and that P_r comes from the area illuminated within the antenna half-power beamwidths β_a and β_e. Thus

$$P_r = \frac{P_t G_{t\max} G_{r\max} \lambda^2}{(4\pi)^3} \int_{-\beta_a/2}^{\beta_a/2} \int_{-\beta_e/2}^{\beta_e/2} \frac{g_t g_r \sigma^o(\theta,\phi)}{R^4} dA \tag{3}$$

where the subscripts a and e refer to the azimuth (H-plane) and the elevation (E-plane) of the antennas (given in Table 1). A narrow-beam assumption is made by considering the variables constant over the illuminated area A_t, then

$$P_r = \frac{P_t G_{t\max} G_{r\max} \lambda^2 \sigma^o A_t}{(4\pi)^3 R_0^4}. \tag{4}$$

To derive the backscatter, (4) is substituted for P_r in (3) to give

$$\sigma_t^o = \frac{R_0^4 \int_{-\beta_a/2}^{\beta_a/2} \int_{-\beta_e/2}^{\beta_e/2} \frac{g_t g_r \sigma_m^o}{R^4} \, dA}{A_I} \qquad (5)$$

where σ_m^o is the measured scattering coefficient and σ_t^o is the true scattering coefficient The gain functions for the mainlobe antenna patterns of the paraboloid and horn antennas approximate to Gaussian functions of the form

$$g(\theta) = e^{\left\{-k\left(\theta/\beta\right)^2\right\}} \qquad (6)$$

where θ is the incidence angle (^{0}) and θ_b is the effective half-power beam-width of the antenna. The constant *k* which describes the circular Gaussian antenna patterns (whose characteristics are given in Table 1) is 2.75, and the form of the beam patterns is shown in Figure 4.

Illuminated Area Calculation

The radar beam projected onto the surface illuminates an area A, in *(6)* changes with θ as a function of range and ship rail height (Figure 4). The spherical Gaussian beam pattern is elongated in the range direction to form an extended ellipse whose dimensions depend on β and θ. For a circular beam projected onto the surface, the area is

$$A_c = \frac{\pi H^2 \beta^2}{4\cos^3(\theta_i)}. \qquad (7)$$

Beam Overlap Correction

The v-pol antennas used for transmit and receive are not perfectly aligned and have non-identical beam patterns. Furthermore, they are separated by a small distance (0.5 m) in the horizontal plane (H-plane). At close range and incidence angles near nadir the beam spot overlap is at its minimum, due to the reduced range and the smaller spot size. The fact that the beam patterns do not overlap perfectly requires a correction to the area A, in the radar equation: the greater the range the larger the beam overlap and the smaller the correction factor. For parallel Gaussian beams this correction factor C_h is (Moore, 1985)

$$C_h = \exp\left\{\frac{-s_h^2 k^2}{\beta_h^2 R_o^2 \left(1 + m_h^2\right)}\right\} \qquad (8)$$

where s_h is the horizontal separation of the antennas, k is a constant, m_h is the ratio of the transmit and receive antenna beam widths and the subscript h refers to the horizontal plane. Each

of the antennas point at identical incidence angles and there is no effective separation in the elevation plane: thus no correction factor is needed for the vertical plane, Figure 4 shows that as incidence angle and range increase, the illuminated area from the narrower parabloid beam becomes increasingly closer to the centre of the collecting horn antenna and the resulting correction factor C_h varies as a function of incidence angle. For a height above the surface of 17m, and values of m_h = 0.35, β_h = 0.139 rad, s_h = 0.5 m, and k = 2.75 (from (6)), C_h increases from -1.15 dB at 20° to a value of -0.23 dB at 65°.

3.4 Data Calibration

During the experiment the radar was to an extent internally self-calibrating. The system contained a loop controlling the period of the calibrator local oscillator source, such that the calibration IF frequency is maintained at 2.5 kHz. The period and center frequency of the internal calibration signal was monitored and recorded using the HP Signal Analyser throughout the experiment in order to document the consistency of the scatterometer measurements.

internal Calibration

Internal calibration during post-processing, uses the 'feed-through' signal to correct for variations in transmitted power. This signal is coupled through the antennas because of finite isolation between transmit and receive antennas. We range-gated the measured signal to isolate the feed-through signal by passing it through a low-pass filter with a cut-off frequency of 1 kHz. We then computed the average power within the filter passband. The daily average of the gated power was within ± 1.5 dB of the mean value from June 25- July 28, 1992 (Julian Days 177- 210), indicating that the radar is relatively stable (see Figure 5a).

In general, returned power from a distributed target varies as $1/R^2$, where R *is* the range to the target. Thus, as the range doubles, the returned power from a distributed target falls-off at 6 dB/octave. However, in our system IF signal passes through a single pole high pass filter with a 6 dB/octave slope to eliminate for R^2 dependence of the received power. The cut-off frequency of the high-pass filter is at 80 kHz. We removed the effect of the IF gain by passing the signal through a low pass filter with the cut-off frequency of 80 kHz. Figure 5b compares the measured backscattering coefficient from sea ice as a function of incidence angle with and without use of the low pass filter. The resulting correction increases the scattering coefficient by up to 4 dB at high incidence angles while reducing it by a smaller amount at low angles.

External Calibration and Signal to Noise

Periodic external calibrations were performed by measuring the received power from a standard 12" Luneberg Lens placed on the surface at varying range. This target was used at several sites throughout the experiment to test the system signal to noise ratio over various ice types and to

enable conversion of power data into scattering coefficients. The theoretical maximum scattering cross-section of the lens (for wavelength $\lambda = 6.98$ cm) is ~11 dBm^2, but performance degradation over its lifetime resulted in a measured reference cross section of 7 dBm^2 (made before the experiment). In addition, the lens is used to obtain a signal to noise ratio (snr) estimate from the system. The ratio of backscatter cross section from a spot of area *A*, to the lens cross-section σ_{lens}, from the radar equation is

$$\frac{P_{in}}{P_{lens}} = \frac{\sigma^o A}{\sigma_{lens}}. \tag{9}$$

If the cross section of the lens σ_{lens} is 7 dBm^2, the peak power in the spectrum from the lens measurement 10 dB, and the illuminated area 10 m^2 (at θ = 450), then the snr can be easily calculated. Rearranging terms in (9) and expressing power in dB

$$\sigma^o_{dB} = P_{,n} - P_{lens} + \sigma_{lens} - 10\log_{10}(A). \tag{10}$$

When the noise floor power P_{noise} *is* substituted for the input power P_{in} then we get a noise equivalent backscatter cross-section Of $\sigma^\circ_{noise} \approx$ -43 dB. For a target of known cross-section such as the lens there is an error in calibration associated with the fact that the measured backscatter σ_m is a combination of the desired field of the target and the surrounding background clutter σ_b. Thus the resulting maximum calibration error is

$$\frac{\sigma_{in} - \sigma_c}{\sigma_c} = \frac{\sigma_b}{\sigma_c} \pm 2\sqrt{\frac{\sigma_b}{\sigma_c}}. \tag{11}$$

If the value of $\frac{\sigma_b}{\sigma_c}$ is -43 dB as estimated above from lens calibrations, then the resulting maximum possible calibration error is ± -18.5 dB, or equivalently about 1 S% error, and is considered negligible.

4. WWGS '92 SCATTEROMETER MEASUREMENTS

The objective of this investigation was to obtain a detailed microwave backscatter signature dataset and to collect validation data for ERS-1 C-band synthetic aperture radar (SAR) observations (at -20 - 26° incidence) of Weddell Sea ice. In this regard, detailed surface measurements were made within the footprint of the radar each time a radar scan was completed. Surface characterisation information comprised snow and ice physical and chemical properties measurements and morphological or structural information.

At short ice stations combined radar and snow and ice measurements were made of a number of

ice types characteristic of the Weddell Sea during the wintertime (Viehoff *et al.*, 1993; Haas *et* a/., 1992). These included undeformed, snow-covered grey (10 - 30 cm thick) and white first-year ice (30 - 70 cm thick), and second-year and former fast ice floes (exceeding 200 cm thickness) each with extreme snow loading. Other deformed ice forms included ridged and rafted white ice and hummocked second-year floes. Of the sites sampled, the following discussion gives a broad description of some typical mean signatures observed during the WWGS '92 transect (Figure 1).

4.1 First-year Ice Signatures

Previous winter C-band signature examples from the Weddell Sea are limited to data from a single field experiment. Observations from WWGS '92 shown in this paper highlight a number of differences, and as anticipated indicate a greater range of signatures than previously documented by Hosseinmostafa *et al.* (1994). Following examples illustrate scatterometer data acquired at individual sites, and a number of mean signatures from collective results from ice with similar salinity, thickness, and roughness characteristics. Graphs showing data from individual sites (with a single measurement set) have points corresponding to the mean of several independent samples at each incidence angle. In cases where averages are constructed from measurements at several sites, symbols indicate the mean values together with error bars corresponding to $\pm 1\sigma$. In either case, a least-squares logarithmic curve is fitted to the mean values to illustrate the trend in the radar backscatter signatures.

Young Ice

Polarstern encountered the ice edge on 10 June, 1992. Extensive pancake ice was observed for the majority of this southbound leg of WWGS'92 as *Polarstern* traversed an extensive marginal ice zone several hundred kilometers wide. A number of pancake ice observations were first made on 12 June with the C-band scatterometer and Figure 1 indicates these locations by crosses along the Greenwich (0°) meridian. Figure 6a shows two distinctly different pancake ice signatures from 13 and 14 June, for similar ice thicknesses of 10-15 cm. The main characteristic of each signature is the fact that there is relatively little fall-off of the radar backscatter with incidence angle: both signatures illustrate extremely high values of σ° exceeding -20 dB at all angles less than 50° incidence. Backscatter at high incidence angles, nonetheless, varies by 15 dB and appears dependent upon; the roughness of the upturned edges of the cakes, the degree of compactness of the ice pans, and the degree of wave washing of the individual ice pans, Pancake ice on 13 June was distinctly different exhibiting greater surface roughness and wave washing, and lower ice concentrations than observed further south on 14 June. Also, in the case of the more southerly location, pancakes had a shallow snowcover which reduces the surface reflection coefficient from values more typical of wave-washed bare pancakes. Drinkwater et *al.* (1993a) show ERS - 1 C-band scatterometer images of [he ice edge in this location during June, also observing that the backscatter at 40° often exceeds -10 dB. Furthermore, it is typical in these

ERS-1 scatterometer images to observe a bright fringe of pancake ice around the outer ice edge of the marginal ice zone in this location due to the higher energy wave environment and the lower ice concentrations.

The consolidation of a young ice sheet into first nilas (<1cm thick) and then grey and white ice was observed in the shore polynya systems along the coast of Antarctica (Figure 1) and along the transect across the Weddell Sea in divergent regions of the ice pack. The average of all white ice observations (of 30 - 70 cm thick ice) is shown in Figure 6b. This mean signature indicates a more rapid fall-off in σ° than data shown by Hosseinmostafa *et al.* (In press) and is likely because these ice are both thinner, smoother and younger than the smoothest first-year ice forms they observed later in the ice-growth season. Many of these white ice observations were made of extremely smooth ice with little rafting or ridging, and the values of σ° of below -25 dB appear typical of the lowermost bracket of backscatter observed by ERS-1 at 20-26° incidence for smooth, young first-year ice (Kwok and Cunningham, 1994). Also of note for this high salinity young ice are low cross-polarized signature of around -40 dB. This appears typical of relatively smooth bodies of recently formed ice which have observed surface salinities of the order of 20 ‰ or higher. The dominance of surface scattering from these smooth, young ice forms also accounts for the relatively rapid decay of σ° with incidence angle of 0.4 dB/deg in the 20-70° range,

Medium-thick first-year ice

By far the most predominant ice form observed throughout the cruise was ice between 50 cm and 75 cm thick. This ice was observed under rapid growth conditions during WWGS '92 in coastal polynya systems. During a period spent stationary in recently formed white ice, this smooth, and fairly undeformed ice was observed to ridge around the vessel during a storm. Measurements were made with the scatterometer both before and after the deformation 'event' and these signatures are compared in Figure 7. The 21 June curve shows a fit to the individual data scan acquired before the storm and the 22 June scan on the following day represents the ridged ice. Surface characteristics and the degree of ridging were inhomogeneous across the transect scanned by the radar, resulting in the variability in the signature values, For comparison, the mean signature of smooth first-year ice throughout the experiment is shown in Figure 8. It demonstrates a more rapid fall-off of 0.6 dB/deg, than the smooth ice in Figure 7, but typical ERS-1 values are of the order of between -10 and -18 dB. Cross-polarized values show little incidence angle dependence, varying between -35 and -38 dB These 20- 26° incidence range values correspond closely with the typical backscattering behaviour of undeformed Arctic first-year ice presented by Kwok and Cunningham (1994). But, the decay in backscatter shows a much steeper fall-off with incidence [ban for comparative ice forms in the Arctic. This mean smooth ice signature is characteristic of ice formed in divergent ice regions away from the coastline, for small characteristic surface roughnesses with standard deviations less than 0.75 cm and correlation lengths of the order of 8.0 cm, This ice form appears typical of the central

Weddell Gyre.

Rough and deformed d first-year ice

The mean signature of rough first-year ice is described by Figure 9a, and is associated with measured forms of deformed medium-thick first-year ice where ridging or rafting is not particularly intense with ridge sail heights generally lower than 1 m. However, this mean signature is biased by way of the fact that little heavily ridged ice was observed during the transect across the central Weddell Sea. Most rough ice forms were observed in the coastal deformation region in the Eastern Weddell Sea which provided little access to the ship, and consequently could not be observed with the scatterometer. Thus, the signature in Figure 9a is not representative of the roughest ice forms observed during WWGS'92 or indeed in the entire Weddell Sea in winter. This translates particularly into low values at the higher incidence angles.

Rough ice shown in Figure 7 indicates the relative extreme observed in more intensely deformed areas of first-year ice, and when compared with Figure 9a indicates the bias to a low mean value at high incidence angles. Nonetheless, the mean backscatter in the ERS- 1 incidence-angle range is between approximately -10 and -16 dB which agrees favorably with the Arctic ERS- 1 observations of deformed first-year ice made by Kwok and Cunningham (1994).

4.2 Second-year Ice

Figure 9 intentionally compares the mean rough first-year ice signature (a) with the mean old ice or second-year ice signature (b). These two mean signatures are extremely similar in character and are almost identical in intensity and gradient. This confirms results shown by Hosseinmostafa et *al.* (1994) who also state that discrimination of first- and second-year ice is difficult on the basis of backscatter magnitude at a specific incidence angle. The only discriminating feature is the that backscatter at higher incidence angles tends to be slightly higher than the mean rough first-year ice signature in Figure 6a. However, this difference would be negligible if examples of rougher first-year ice had been sampled. Notwithstanding this observation, all old floes observed during WWGS'92 had extremely deep, layered snow covers (exceeding 1 m in depth), similar to cases previously observed by Wadhams *et al.* (1987). Volume scattering from the snow upon older sea ice is responsible for the higher incidence angle backscatter, in direct contrast to the ice-surface scattering occurring from the rough first-year floes in Figure 9a.

5. ERS-1 CALIBRATED BACKSCATTER RESULTS

Calibrated SAR- and Scatterometer-de rived, incidence-dependent σ^{o} values from the ERS-1 Active Microwave Instrument (Drinkwater et *al.*, 1994) show good correspondence with the results shown in the previous section. figure 10 shows a summary of SAR image histogram

statistics derived from 3 regions of contrasting ice conditions in the Weddell Sea from Drinkwater *et al.*. (1994). These correspond in Figure 1 to locations of deformed coastal first-year ice in the Eastern Weddell Sea (i.e. rough first-year); undeformed white ice in the central Weddell Gyre (i.e. smooth first-year); and a region of mixed deformed first-year, undeformed medium first-year and second-year ice (i.e. first-year/second-year) in the north-western Weddell Sea, Drinkwater et *al*.. show the locations of the sample areas described in Figure 10 at; 72° S 13°W; 67° S 26°W; and 64° S 42°W, for rough first-year, smooth first-year, and mixed ice respectively. Peaks in each of the two component distributions closely reflect the 20- 26° incidence angle field scatterometer data values shown in the previous section, These data appear to show that the mixed deformed and undeformed histogram is a simple convolution of the individual distributions of the components of first-year and second-year ice (or deformed first-year ice) in proportions determined by their relative concentration.

ERS- 1 backscatter data indicate that discrimination of rough first-year and second-year ice is difficult due to similarities in their backscatter in the 20-26° range. ERS- 1 observations and field scatterometer measurements shown in this paper support this conclusion. However, discrimination of thick versus thin ice is a more critical task from the perspective of estimating ice mass or freshwater flux in the Weddell Sea. Scatterometer signatures and ERS- 1 SAR histograms appear to demonstrate that discrimination of the principal categories of thick deformed first-year (or second-year) and smooth undeformed first-year or white ice is a fairly simple task. Multiple incidence angle measurements made by a scatterometer are also more adept at separating ice types than the limited incidence angle range provided by ERS-1 SAR. Scatterometer measurements may therefore be more valuable for monitoring the areal extent of relatively thick and thin ice (Grenfell et *al*., 1992; Martin et *al.*, 1992). In contrast, SAR enables more detailed high resolution estimates of the lead fraction or amount of undeformed versus deformed ice in a given region, or indeed tracking of this ice through the growth season (Drinkwater and Kottmeier, 1992).

6. TIME-SERIFS RESULTS

A 3-day long ice station from 21-24 July, 1992 offered the possibility of making time-series observations of 1 m thick smooth, first-year sea ice with the field scatterometer. In addition to periodic scans of data over the complete range of incidence angles, the radar was operated at frequent intervals (~4 hourly) at a fixed incidence angle of 45°, and at both polarisations. The angle was chosen because the radar responds sensitively to the surface reflectivity and roughness, and is also sensitive to volume scattering from the snow and ice surface layers.

Large temperature changes recorded during the ice station drift enabled an investigation of the

links between microwave signature characteristics and the meteorological conditions controlling the surface-energy balance. For determination of the energy budget, the University of Hannover continuously measured the radiation budget, turbulent fluxes of sensible and latent heat, and the conductive heat flux through the sea ice and snow cover (see Lemke, 1994; pages 40-49) for a total of over 60 hours of data (courtesy of W. Frieden of Hannover University, Germany). Measurements of the incoming short- and long-wave radiation were made with a CM-11 Kipp and Zoenen pyranometer and Epply pyrgeometer, respectively. Outgoing long-wave radiation was measured with a KT-4 radiation-thermometer and reflected short-wave with a downward-looking pyronometer, so that the albedo can be directly calculated. Turbulent fluxes were characterised using measurements from a Metek sonic anemometer thermometer mounted on the ship's boom. A series of 10-minute averages are computed from the original 10 Hz sampled data stream, which yield direct estimates of the kinematic wind stress and the components of the wind, and a measure of the turbulent flux of sensible heat.

In Figure 11, data are compared for a period when the net radiation budget shows a large transition. Field experiment data records illustrate 10 minute averages of wind stress and turbulent sensible heat flux together with the net energy budget during a C-band radar scatterometer time-series of measurements between days 203 and 206 (21 to 24 July, 1992). In the lowermost panel of Figure 11 the 450 incidence mean C-band signature is plotted starting at Julian Day 203.79. The solid line represents the mean vv-polarized backscatter (σ^o_{vv}) with error bars indicating the true range of variability of independent data samples, and the dashed line shows the corresponding mean hv polarized backscatter (σ^o_{hv}). A 10 dB variation in σ^o_{vv} and 5 dB variation in σ^o_{hv} is observed in response to the changes in the heat fluxes presented.

Figure 11a indicates a large variation in wind stress during this period, increasing rapidly to over 0.5 N/m^2 when the winds peaked at 20 m/s. The increase in wind took place with a large rise in air temperature (Figure 1 lb) from around -23° C to O°C, during the passage of a warm front. As a consequence of the overcast skies, warm temperatures and the high wind, the sonic-anemometer-thermometer recorded a net negative (downward/incoming) flux of sensible heat which peaked during the strong winds at 60 W/m^2. Later, a sharp decrease in the amount of incoming turbulent sensible heat occurs on the morning of 24 July, due to the clear night sky.

A net energy budget (F_{NET}) is shown in Figure 1 1c as a solid line, using the conventional system of negative net outgoing flux of heat and positive net incoming heat flux. The largest measured components of this budget are indicated as; the net radiative flux (Q); the net sensible heat flux (H); and the conductive heat flux (F_{COND}). At the start of the period, the surface lost nearly 50 W/m^2 in radiative and sensible heat with this loss balanced largely by conducted heat. Some heat is supplied by the freezing at the base of the ice sheet, as indicated by ice core measurements and a thermistor chain frozen into the sea ice. Immediately the sky became overcast on day 204

temperatures rise and light snowfall began. Radar data (Figure 1 ld) indicate several orders of magnitude variability in backscattering over the conditions experienced during the following period. The change in heat flux regime is strongly correlated with a reduction in vv and hv backscatter as the net radiative and sensible heat flux (Q+H) swings from outgoing to incoming. At first conduction takes care of the surface warming, carrying heat away from the snow and ice surface until the time at which the ice sheet becomes nearly isothermal (at day 205.5), Melting (hen begins to wet the snow surface and the backscatter rapidly rises to its peak. Subsequently, high winds and a brief period of cloud-free night at Julian Day 206.25 encourage evaporative cooling, a minimum in F_{NET}, and a local minimum in the values of vv and hv-pol backscatter.

Surface measurements in association with the C-band radar data indicate that the vv-polarized data clearly signal the change in heat flux environment when air temperatures rise above -20°C. As surface temperatures rose dramatically, snow-grain transformations begin and equi-temperature metamorphism is first focused at the surface, reducing the large angular grains to small rounded grains. As the warm temperatures penetrate down to the ice surface the previously exaggerated snow temperature gradients become reduced. However, the wind speed continues to rise to gale force. The σ^o_{vv} reduction minors the rise in Q+H in Figure 1 lc, reaching a minimum below -35 dB. A reversal then occurs in σ^o_{vv} with a rise in backscatter values up to a level higher than that on day 203. During this period, no significant amount of surface wetness accumulated in the shallow 3 cm deep snow layer until the latter part of day 205. Instead, the wind speeds at the surface were large enough that sufficient heat is removed by surface sublimation or conduction to prevent visible melting and free-water appearance in the snow (as described by Andreas and Ackley, 1982). Until after day 205.5, it is suggested that in the case of these strong winds enough heat is removed to preclude significant melting. The large change in thermal profile in the snow rapidly changed snow crystal characteristics under these conditions from hoar-style angular crystals (induced earlier by strong negative heat gradients before day 204) to rounded crystals. Together with the layering which developed in the snow, it is proposed that these snow changes play a large role first by reducing and then subsequently by increasing volume scatter as rounded grains grow larger. The last significant change in σ^o_{vv} takes place after cooling and overnight refreezing (day 206) of moisture in the snow layer upon a brief reversal of the net heat budget from positive to negative. Diurnal cooling and the swing in the humidity during this period on day 206 result in a brief minima in σ^o_{vv}. The rapid return to values above -30 dB coincide with the brief period of incoming short-wave energy during scattered clouds at mid-day and signifies the reappearance of moisture at the surface of the snow.

This winter example clearly indicates that the sea-ice surface properties respond to the balance of fluxes at the surface. Furthermore, C-band values of σ^o_{vv} react equally sensitively to these changes. Though these temperature swings may be more commonly associated with spring conditions, this change in events may be recognized in time-series data to reflect transformations

in the surface heat and vapour flux environment. It is proposed that with the aid of buoy data and weather analysis fields (for specifying boundary conditions), satellite radar and surface data be used together with physical models to understand how microwave data reflect key changes in the energy balance. The power of such time-series measurements using SAR backscatter has barely been exploited. Coupling data analyses in this manner together with the tracking capability of SAR provides a powerful method for studying geophysical processes and surface changes (Drinkwater, In Press).

9. CONCLUSIONS

More widespread field scatterometer measurements are required before Antarctic sea ice in the Southern Ocean are equally as well characterised as Arctic sea ice in terms of frequency- and polarisation-dependent microwave backscattering characteristics of different ice forms. Despite these shortcoming, data illustrate sea ice in the Weddell Sea to be somewhat unique in terms of its microwave backscattering signatures and there is clearly much useful information to be derived by exploiting the satellite C-band satellite data in this remote part of the globe. Japanese SAR data may, for instance, also be acquired to illustrate L-band backscattering characteristics of Southern Ocean Sea ice in future studies.

Winter scatterometer data samples from relatively thin first-year ice growth forms, and thicker deformed frost-year ice or second-year ice forms are distinguishable, thus providing a method for identifying leads or relatively thin ice and therefore locations within the ice-pack where ocean-ice-atmosphere heat exchange is significant. Comparisons with calibrated ERS-1 scenes show that these backscatter differences in the 20-260 incidence angle range can be used to discriminate thin and thick ice fairly effectively.

Time-series examples of the C-band signatures show how the time dimension can then be used to identify periods of key changes in the surface flux environment. When coupled with surface temperature measurements, periods of net positive heat fluxes may be distinguished from net negative heat fluxes to identify periods of more vigorous heat exchange and ice growth. This is of particular interest in the Antarctic since surface melting does not always take place when the surface heat flux becomes positive. The dynamic range experienced by the scatterometer power measurement during such cycling of the heat fluxes indicates that significant information is contained at higher incidence angles such as 45°, in the range where both surface scattering and volume scattering have significant influence upon observed signatures. A more complete characterisation of the backscatter relationships with both SAR and ERS-1 wind scatterometer data, with methods described by Drinkwater et *al.* (1994), is therefore of particular interest in this regard. Establishment and refinement and of a methodology for wide-scale application of long-term spaceborne radar monitoring techniques is essential to the capability for estimation of the

surface fluxes of the Weddell Sea and particularly the impact of (he entire Southern Ocean on global atmospheric and oceanographic conditions. Once relationships between microwave signatures, geophysical properties and surface fluxes are understood in different heat flux regimes, estimates may be extrapolated to larger scales over the Southern Ocean.

8. ACKNOWLEDGMENT

Special thanks go to Robert Bruce for his efforts in preparing the data acquisition programs, and Wolfgang Dierking for support of the field measurements and in solving technical problems. Christian Haas, Alan Lohanick, Robert Massom and Markus Thomas are thanked for their untiring snow and ice data acquisition, Wolfgang Frieden of Hannover University and Christian Wamser of AWI kindly provided radiation and surface flux data, and Thomas Viehoff and Peter Lemke supported field measurement planning. M.R.D. carried out this work at the Jet Propulsion Laboratory, California Institute of Technology under contract to the National Aeronautics and Space Administration.

9. REFERENCES

ANDREAS, E.L., and S.F. ACKLEY, 1982, On the differences in Ablation Seasons of Arctic and Antarctic Sea Ice, *J. Atmospheric Sci.*, *39, 440-447.*

CARSEY, F. D., 1980, Microwave Observations of the Weddell Sea Polynya, *Monthly Weather Review,* 108,2032-2044.

CARSEY, F. D., R.G. BARRY, and W.F. WEEKS, 1992, Introduction, In *Microwave Remote Sensing of Sea Ice,* (Ed.) F.D. Carsey, AGU *Geophysical Monograph ,28,* 1, 1-7.

DRINKWATER, M. R., In Press, Applications of SAR Measurements in Ocean-Ice-Atmosphere Interaction Studies. In *Oceanographic Applications of Remote Sensing,* (editors) Ikeda, M. and Dobson, F., Chapter IV-A-3., CRC Press.

DRINK WATER, M. R., and C. KOTTMEIER, 1994, Satellite Microwave Radar- and Buoy-tracked Ice Motion in the Weddell Sea during WWGS'92. Paper submitted to *Proc. IGARSS '94,* Pasadena, CA, Aug. 8-12.

DRINKWATER, M. R., D.S. EARLY and D.G. LONG, 1994, ERS-1 Investigations of Southern Ocean Sea-ice Geophysics using Combined Scatterometer and SAR Images. Paper submitted to *Proc. IGARSS '94,* Pasadena, CA, Aug. 8-I?.

DRINKWATER, M. R., D. G. I. ON(i, and D.S. EARLY, 993a, Enhanced Resolution Scatterometer Imaging of Southern Ocean Sea Ice, *ESA Journal,* 17,307-322,

DRINKWATER, M. R., HOSSEINMOSTAFA, R., and W. DIERKING, 1993b, Winter Microwave Radar Scatterometer Sea Ice Observations in the Weddell Sea, Antarctica. *Proc. IGARSS* '93, Tokyo, Japan, Aug. 18-21, Vol. 2,446-448.

GOGINENI, S., R.K. MOORE, Q. WANG, A. GOW, and R.G. ONSTOTT, 1990, Radar Backscatter measurements over saline ice, *Int. J. Remote Sensing, 11,603-615.*

GORDON, A., 1991, Two stable modes of Southern Ocean Winter Stratification, P.C. Chu and J.C. Gascard (Eds.), Deep *Convection and Deep Water Formation in the Oceans,* Elsevier Science Publishers, 17-35.

GORDON, A. and B. A., HUBER, 1990, Southern Ocean Winter Mixed Layer, *J. Geophys. Res.,* 95, 11655-11672, 1990.

GRENFELL, T. C., D.J. CAVALIER], J.C. COMISO, M.R. DRINKWATER, R.G. ONSTOTT, 1. RUBINSTEIN, K. STEFFEN, and D.P. WINEBRENNER, 1992, Microwave Signatures of New and Young Sea Ice, In *Microwave Remote Sensing of Sea Ice*, (editor) F.D. Carsey, American Geophysical Union, Geophysical Monograph 28, Chap. 14, 291-301.

HAAS, C., T. VIEHOFF, and H. EICKEN, Sea Ice Conditions during the Winter Weddell Gyre Study 1992 ANT X/4 with R/V Polarstern: Shipboard Observations and AVHRR imagery, *A WI Berichte aus dem Fachbereich Physik, 34,* Alfred Wegener Institut fur Polar- and Meeresforschung, Dec. 1992.

HOSSEINMOSTAFA, R., V.I. LYTLE, K.C. JEZEK, S.P. GOGINENI, S.F. ACKLEY, and R.K. MOORE, In Press, Comparison of Radar Backscatter from Antarctic and Arctic Sea Ice, *J. Electromagnetic Wave and Applications.*

KWOK, R. and G.F. CUNNINGHAM, 1994, Backscatter Characteristics of the Winter Ice Cover in the Beaufort Sea, *J. Geophys. Res.,* **99** (C4), 7787-7802.

LEMKE, P. (editor), 1994, The Expedition ANTARKTIS X/4 of R/V "Polarstern" in 1992, Reports on Polar Research, 140, Alfred-Wegener-Institut fur Polar- und Meeresforschung, D-27568, Germany, 90pp.

MARTIN, S., K. STEFFEN, J. COMISO, D. CAVALIERI, M.R. DRINKWATER, and B.

HOLT, 1992, Microwave Remote Sensing of Polynyas, In *Microwave Remote Sensing of Sea Ice*, (editor) F.D. Carsey, American Geophysical Union, Geophysical Monograph 28, Chapter 15, pp. 303-311.

MOORE, R. K., 1985, Effect of Pointing Errors and Range on Performance of Dual-Pencil-Beam Scatterometers, *IEEE Trans. Geosci. and Remote Sens.*, *GE-23, 6,901-905.*

VIEHOFF, T., W. DIERKING, CH. KOTTMEIER, and M.R. DRINKWATER, 1993, Sea ice characteristics in the Weddell Sea as observed by ERS- 1 SAR, AVHRR, and ground-based measurements, Paper submitted to *Proc. European Geophysical Society XVIII General Assembly*, Wiesbaden, Germany, 3-7 May.

WADHAMS, P., M.A. L. ANGE, and S.F. ACKLEY, 1987, The ice thickness distribution across the Atlantic sector of the Antarctic Ocean in mid-winter, *J. Geophys. Res.*, **92, 14,535-552.**

TABLES

Table 1. System Specifications

Make:	King KRA 405 Radar		
Type:	Frequency Modulated Continuous Wave (FM-CW)		
Power Requirement:	28 VDC capable of 1.5 AMP output		
Transmitter Power:	150 mW		
Center Frequency:	4.3 GHz ± 1S MHz		
RF Bandwidth:	100 MHz		
Max/Min Hi/Lo Logic:	+10V --- +2V		
Polarization:	VV, HV		
Antennas:	Parabolic Transmit, Horn Receive (linear pol)		
	Flat Plate KA 54 antenna (cross pol)		
Antenna Beamwidths:			
Transmitting (linear pol)	Parabolic:	E-plane;	circular Gaussian pattern
	46cm diam.	H-plane;	8° beamwidth
Receiving (linear pol)	Horn:	E-plane;	23° elevation
	Ncm x Ncm	H-plane;	22° azimuth
(cross pol)	KA 54:	E-plane;	50*5°
		H-plane;	40*4°
Calibration: Internal	Signal Injection (delay line)		
External	12" Luneberg-lens reflector		
Target Range:	15m - 60rn		

FIGURES

Figure 1. Weddell Sea study region showing shipborne scatterometer measurement locations and ice types.

Figure 2. Radar scatterometer mounted on port rail of *Polarstern* during WWGS '92,

Figure 3. 4.3 GHz FM-CW Radar Block Diagram.

Figure 4. (a) Antenna patterns of the v-pol transmitting and receiving antennas; and (b) illuminated area and beam-overlap on the surface (to scale).

Figure 5. (a) Internal 'feed-through' power variations over the period of WWGS '92 measurements; and (b) illustration of the IFGain correction as a function of incidence angle.

Figure 6. (a) Pancake ice signature comparison between 13 and 14 June, 1992 near the ice margin; and (b) mean White ice signatures at vv- and hv-polarizations.

Figure 7. Comparison of medium first-year ice signatures at the same location (a) on 21 June, 1992- before ridging (smooth), and (b) on 22 June - after ridging (rough),

Figure 8. Mean backscatter signature from combined measurements of smooth, medium-thick first-year ice.

Figure 9. Comparison of mean vv-pol. backscatter signatures of (a) rough first-year, and (b) second-year ice.

Figure 10. ERS- 1 calibrated SAR backscatter distributions for; rough first-year (FYR); smooth first-year (FYS); and mixed first- and second-year ice (FY/SY).

Figure 11. Shipborne C-band microwave radar scatterometer time-series comparison with surface fluxes of heat and momentum. (a) turbulent flux of momentum; (b) turbulent flux of sensible heat; (c) the energy balance (d) vv and hv backscatter response with temperature and humidity. Data were acquired during the Winter Weddell Gyre Study in the austral winter of 1992.

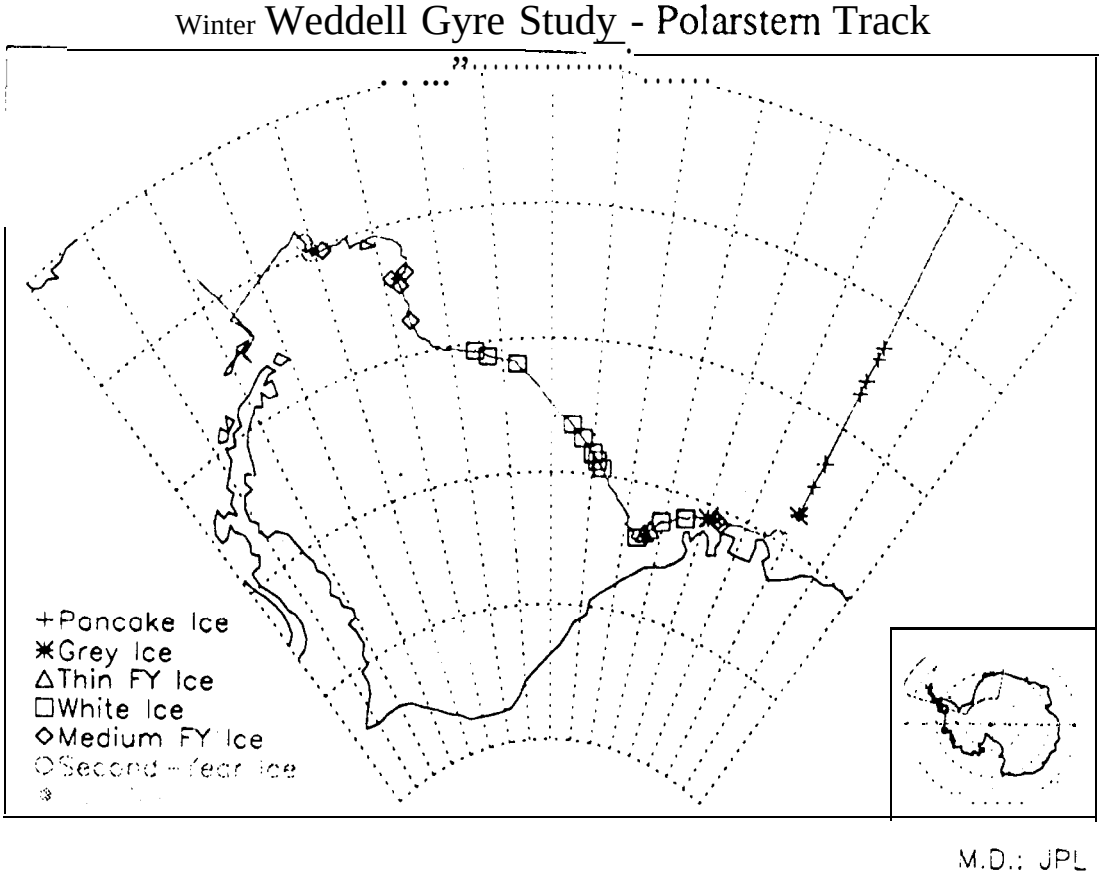

Figure 1. **Weddell** Sea study region showing **shipborne scatterometer** measurement locations and ice types.

FIGURE 2

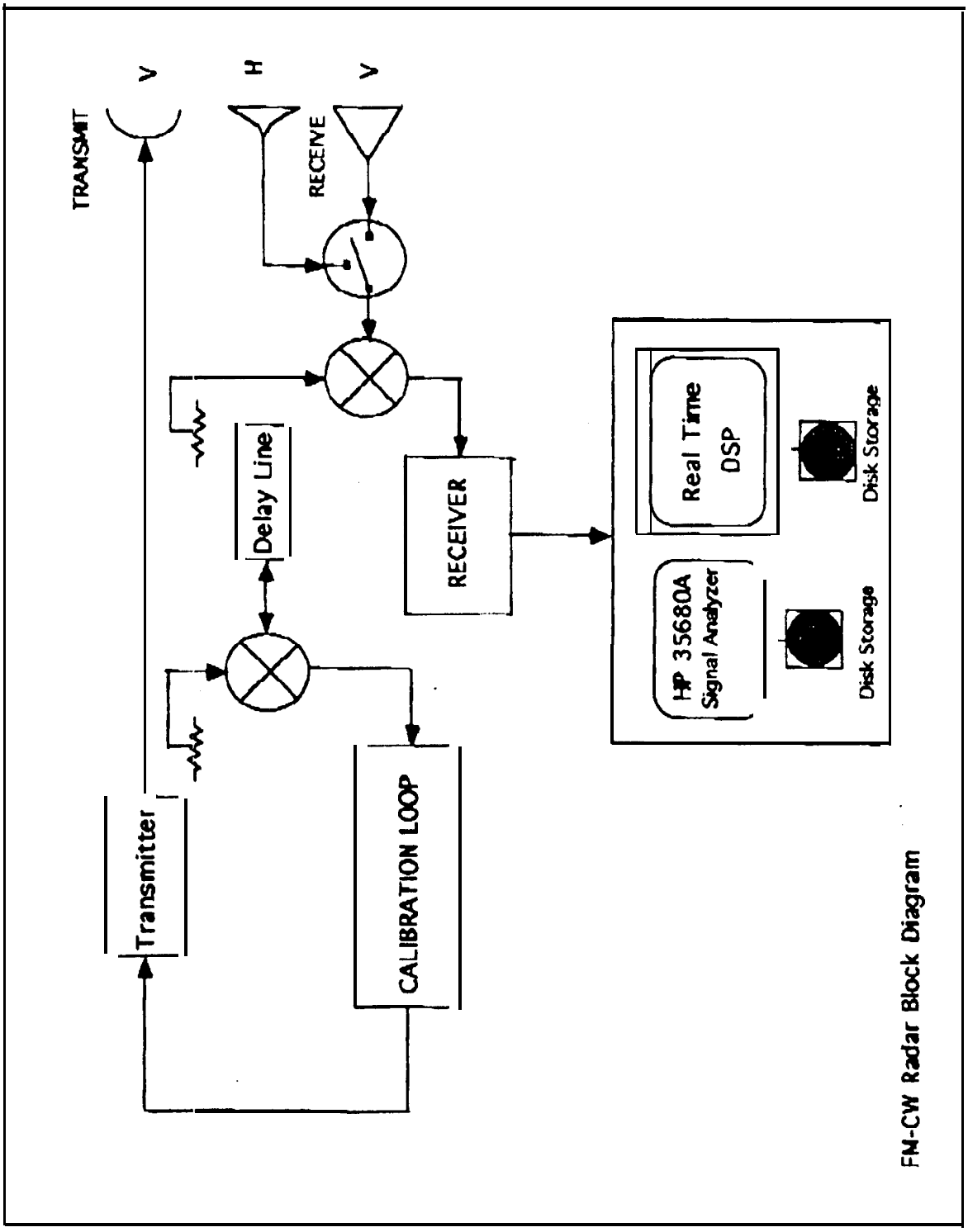

Figure 3. 4.3 **GHz FM-CW Radar** Block Diagram.

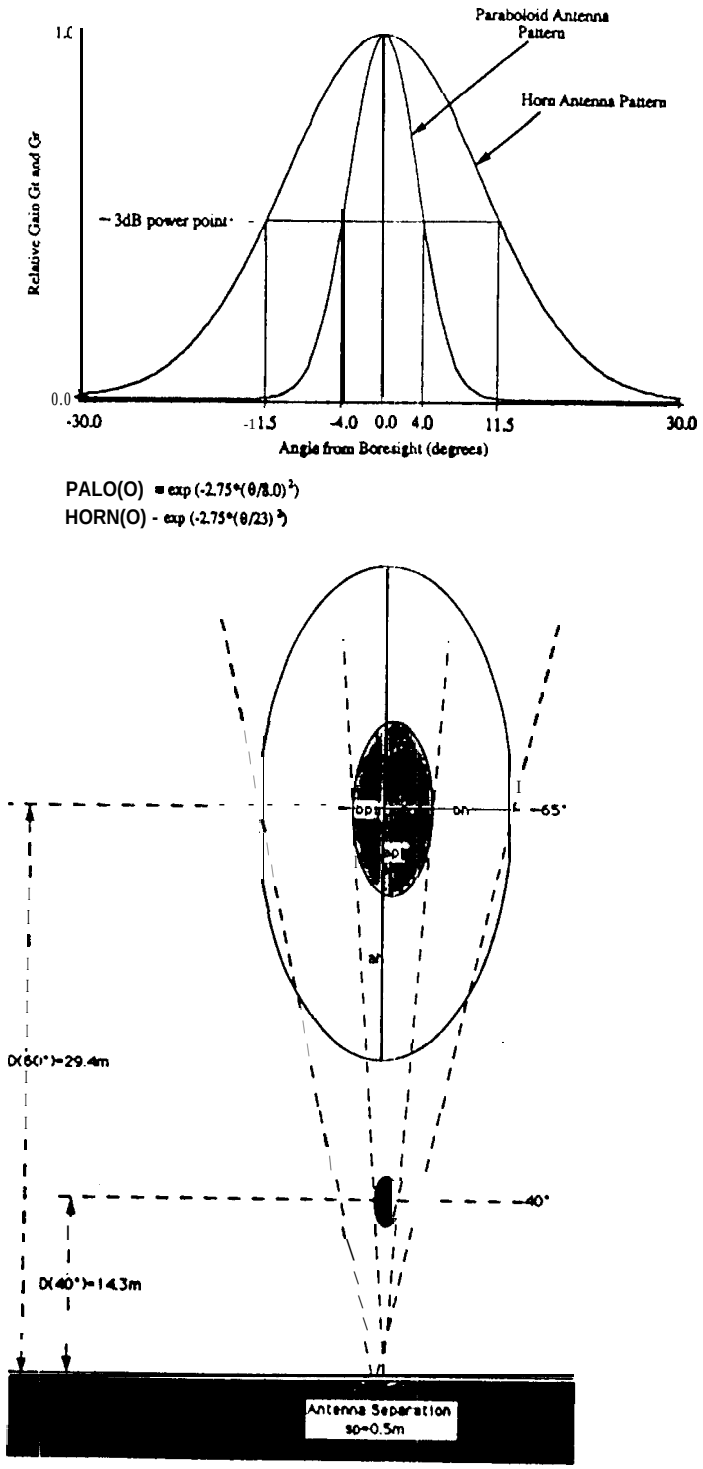

Figure 4. (a) Antenna patterns of the v-pol transmitting and receiving antennas; and (b) illuminated area and beam-overlap on the surface (to scale).

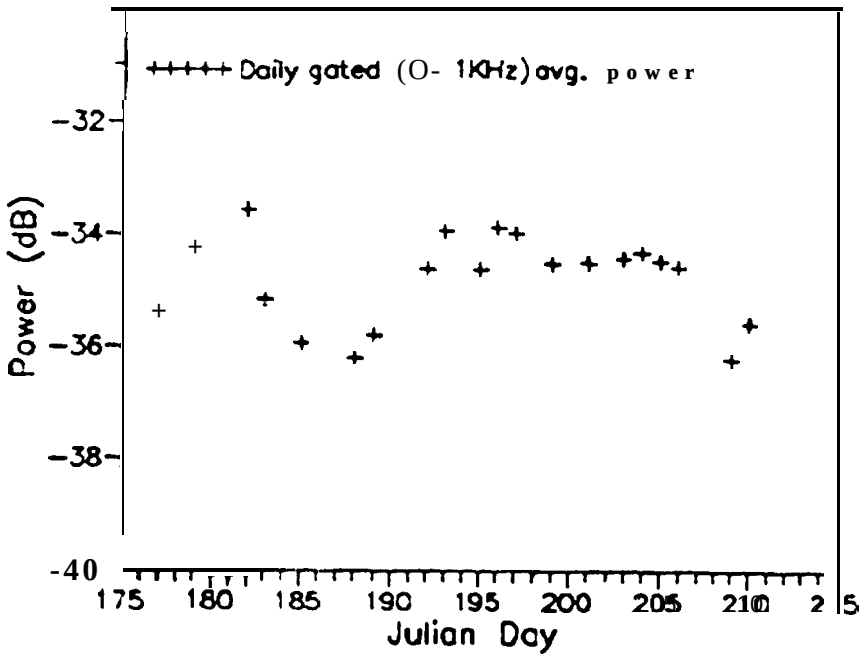

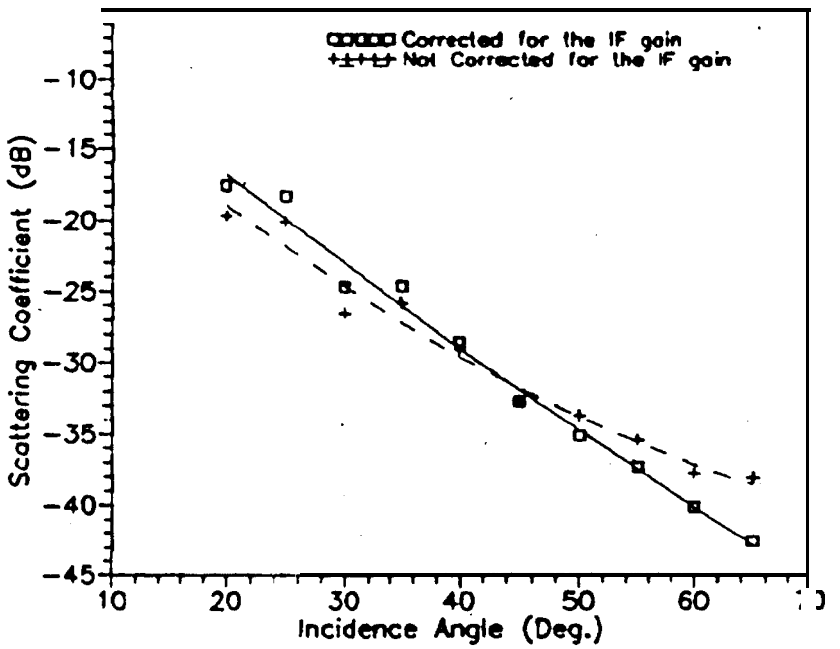

Figure 5. **(a)** Internal 'feed-through' power variations over the period of WWGS '92 **measurements; and** (b) illustration of the **IF** Gain correction as a **function** of incidence angle.

a.

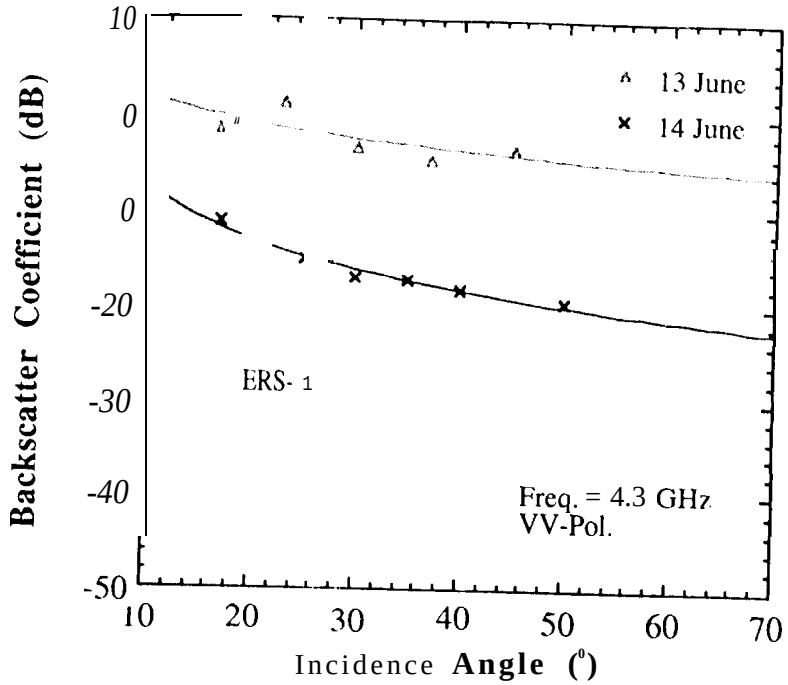

b.

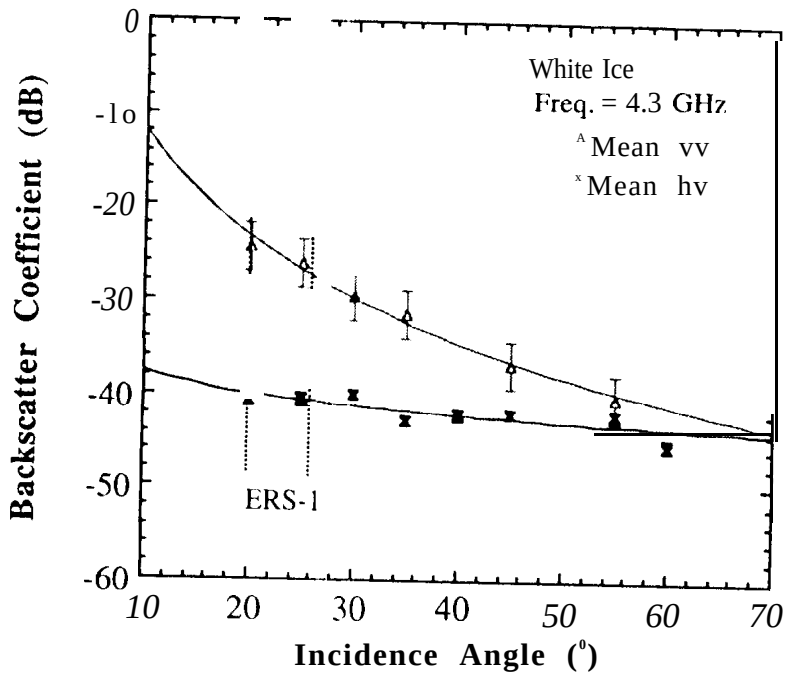

Figure 6. (a) Pancake ice signature comparison between 13 and 14 June, 1992 near the ice margin; and (b) mean White ice signatures at vv- and hv-polarizations.

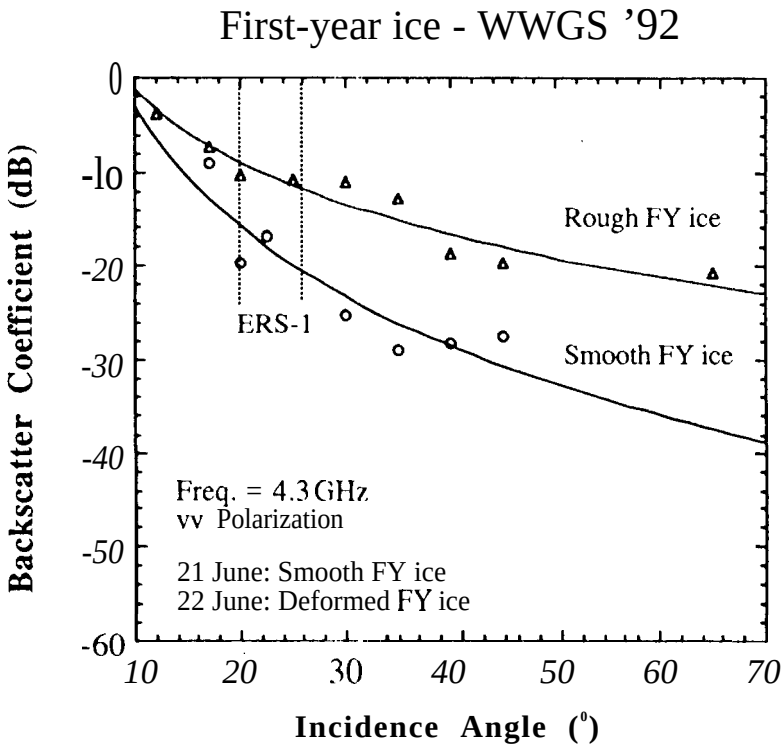

Figure 7. Comparison of medium first-year ice signatures at the same location (a) on 21 June, 1992- before ridging (smooth), and (b) on 22 June - after ridging (rough).

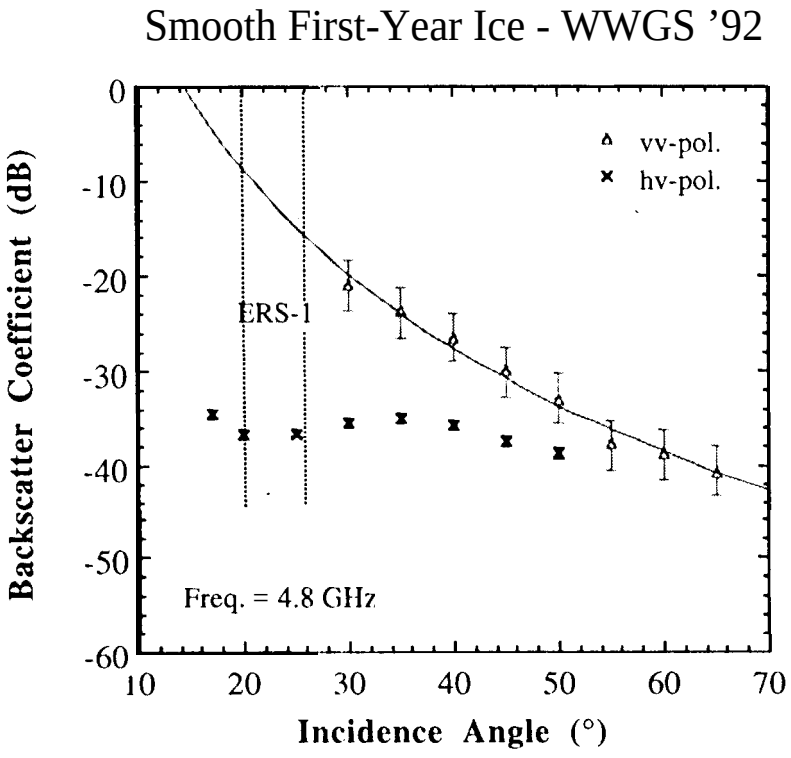

Figure 8. Mean backscatter signature from combined measurements of smooth, medium-thick first-year ice.

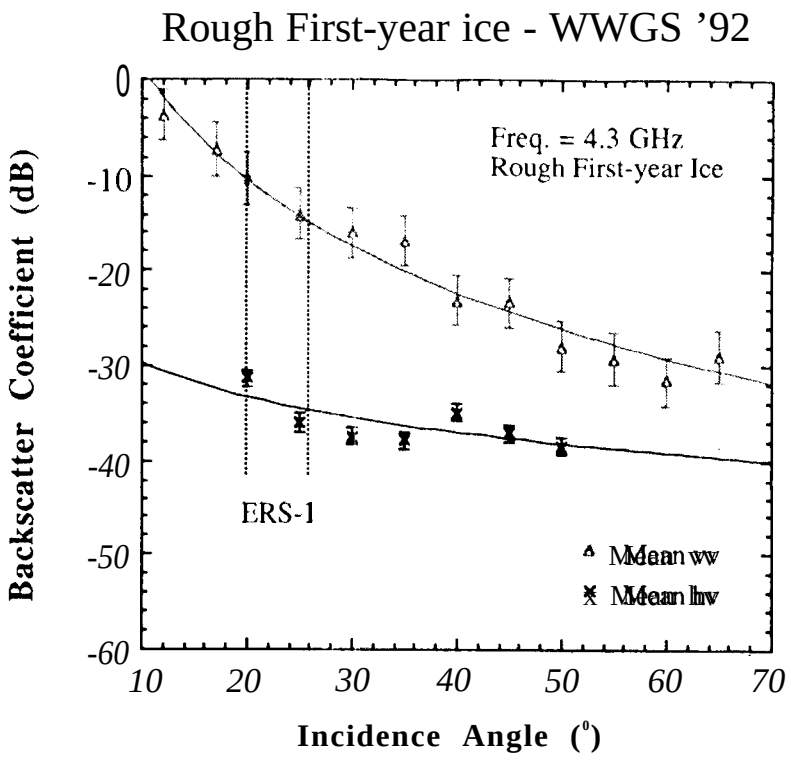

b.

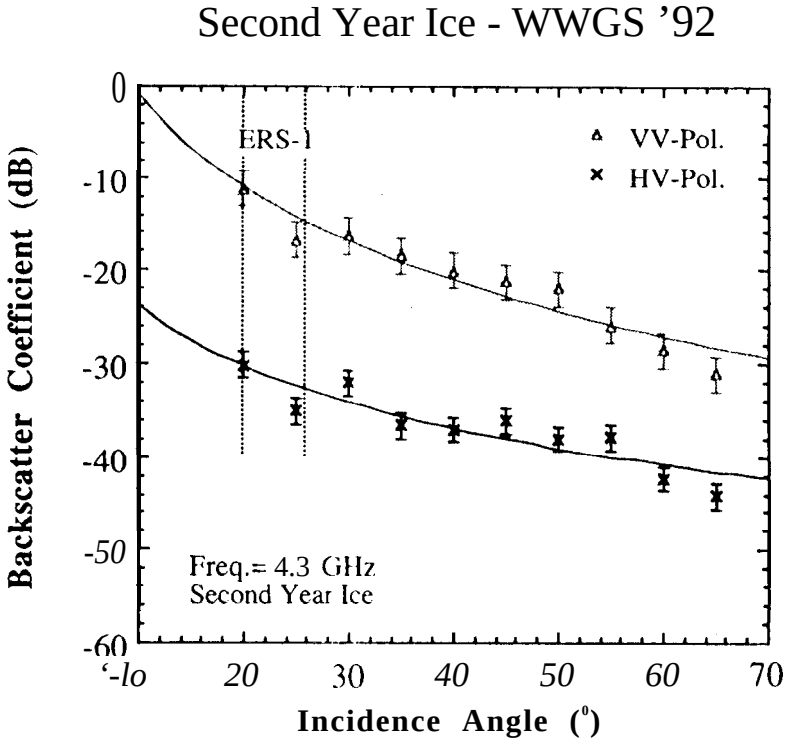

Figure 9. Comparison of mean vv-pol. backscatter signatures of (a) rough first-year, and (b) second-year ice.

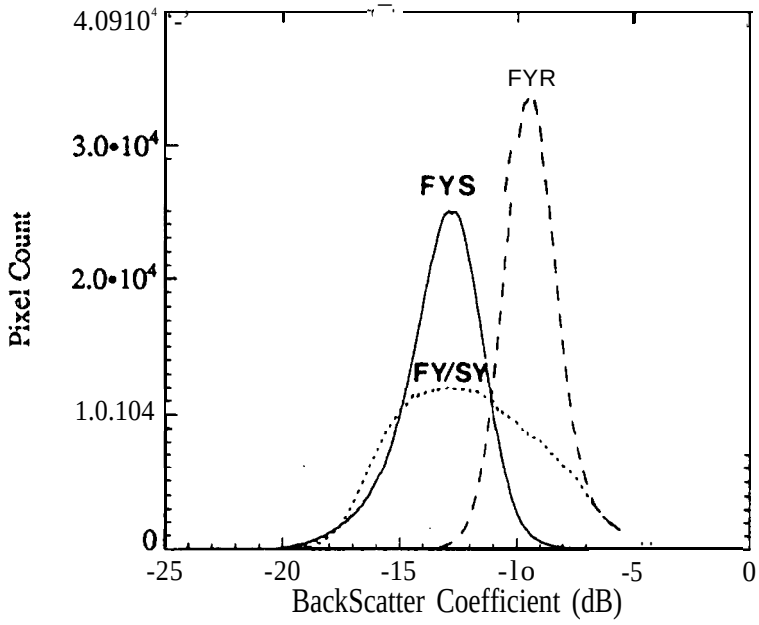

Figure 10. ERS-1 calibrated SAR backscatter distributions for; rough first-year (FYR); smooth first-year (FYS); and mixed first- and second-year ice.

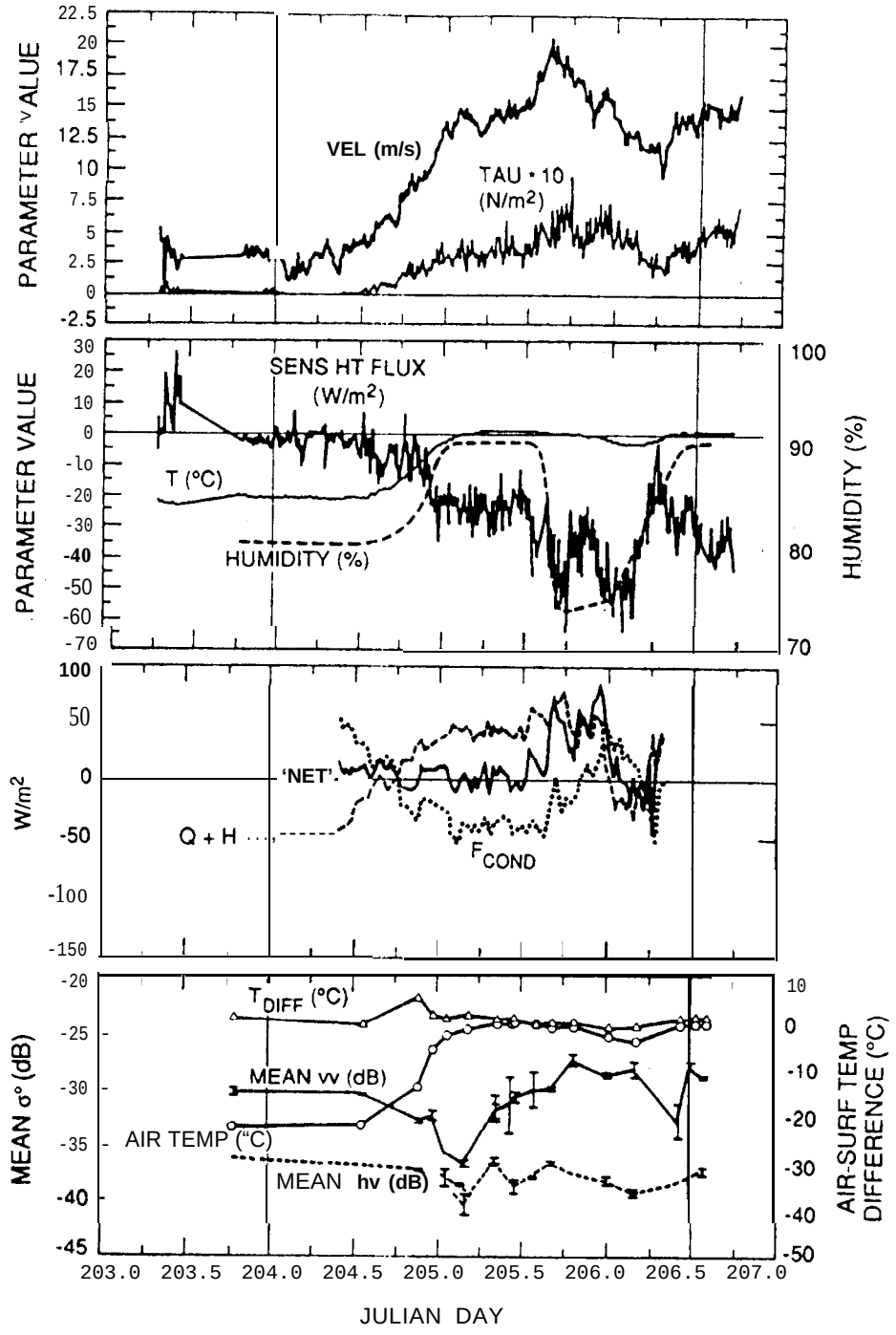

Figure 11. Shipborne C-band microwave radar scatterometer time-series comparison with surface fluxes of heat and momentum. (a) turbulent flux of momentum; (b) turbulent flux of sensible heat; (c) the energy balance (d) w and hv backscatter response with temperature and humidity. Data were acquired during the Winter Weddell Gyre Study in the austral winter of 1992,